www.aem-journal.com

Electrode Placement Optimization for Electrical Impedance Tomography Using Active Learning

Junhyeong Lee, Kyungseo Park, Kundo Park, Yongtae Kim, Jung Kim,* and Seunghwa Ryu*

Electrical impedance tomography (EIT) offers a versatile imaging modality with a multitude of applications, although it encounters accuracy limitations. Herein, a novel systematic framework is presented that integrates a neural network (NN), active learning, and transfer learning to optimize electrode placement, improving image reconstruction performance based on userdefined metrics. Given the many-to-one mapping between electrode configuration and the performance metric, the approach utilizes a NN that predicts performance metrics from electrode placement input. To maintain NN's prediction accuracy for unseen electrode configurations, performance metrics are maximized while iteratively updating the NN via active learning during the optimization process. Transfer learning is employed to expedite optimization of electrode placements for time-consuming iterative reconstruction techniques by fine-tuning a NN initially trained on one-step reconstruction data. The method is validated using two representative reconstruction methods: one-step reconstruction with Newton's one-step error reconstructor prior and the iterative total variation method. This research underscores the potential of the proposed framework in addressing EIT's inherent limitations and augmenting its performance across diverse applications and reconstruction methods. The framework could potentially contribute to the advancement of noninvasive medical imaging, structural health monitoring, strain sensing, robotics, and other fields that depend on EIT.

J. Lee, K. Park, Y. Kim, J. Kim, S. Ryu Department of Mechanical Engineering Korea Advanced Institute of Science and Technology (KAIST) 291 Daehak-ro, Yuseong-gu, Daejeon 34141, Republic of Korea E-mail: jungkim@kaist.ac.kr; ryush@kaist.ac.kr

K. Park
Department of Robotics and Mechatronics Engineering
Daegu Gyeongbuk Institute of Science and Technology (DGIST)
333 Techno Jungang-daero, Hyeonpung-eup, Dalseong-gun, Daegu
42988, Republic of Korea

The ORCID identification number(s) for the author(s) of this article can be found under https://doi.org/10.1002/adem.202301865.

© 2024 The Authors. Advanced Engineering Materials published by Wiley-VCH GmbH. This is an open access article under the terms of the Creative Commons Attribution-NonCommercial License, which permits use, distribution and reproduction in any medium, provided the original work is properly cited and is not used for commercial purposes.

DOI: 10.1002/adem.202301865

1. Introduction

Electrical impedance tomography (EIT) is a method for determining the conductivity distribution within a specific area by using voltage measurements from a limited number of electrodes. EIT was initially developed for medical imaging purposes, with the aim of monitoring the health of the human body's organ system, owing to its noninvasive, safe, durable characteristics.^[1,2] These features of EIT have enabled its application to various fields beyond its original application such as structural health monitoring,[3] strain sensing, [4] and robotics. [5,6] Particularly, there has been a noticeable increase in the use of conductive composite materials for the monitoring and prediction of structural damage in building materials.^[7-12] Additionally. with the emergence of 3D printing capabilities for such materials, there are anticipations of significant expansion in the application of this technology. [13,14] Despite its usefulness, EIT has intrinsic limits in producing highaccuracy conductivity images due to its diffusive nature and a constrained dimension of voltage measurements. To address this challenge, researchers have explored var-

ious approaches, such as upgrading image reconstruction methods through the incorporation of more prior knowledge or making better use of the given voltage data. [5,6,15] Additionally, some studies have focused on finding better current stimulation and voltage measurement patterns to improve the reconstruction ability of EIT. $^{[16-18]}$

Another promising approach is adjusting the electrode placement to enhance image accuracy, especially when utilizing additional electrodes is not feasible due to the restricted number of available electrodes. Recent advancements in machine learning have facilitated the development of systematic approaches for optimizing electrode placement in EIT.^[19–21] For instance, Park et al. applied a neural gas algorithm, an unsupervised learning method typically used for clustering and pattern recognition, to minimize the portion of the blind spot where the current from electrodes cannot reach.^[19] While this method can offer optimal electrode placements for general EIT applications, it may not be suitable for identifying optimal placements under specific conditions, such as image reconstruction objectives, reconstruction methods, and driving patterns. The objective of reconstruction can vary, encompassing position description, ^[22,23] size description, ^[24,25] and shape

ENGINEERING

www.advancedsciencenews.com www.aem-journal.com

description, [26,27] while the choice of reconstruction method may depend on the specific application context. [28] Consequently, optimizing electrode placement to align with particular objectives and circumstances is important for enhancing EIT's reconstruction accuracy. Smyl and Liu^[20] introduced an alternative approach that employs a neural network (NN) to predict electrode placement based on metrics evaluating the performance of the configuration. The NN-based prediction model offers the advantage of determining optimal electrode placement for any user-defined metric and context, provided the network is trainable. Despite this, the study's implementation of an inverse modeling network, which utilizes reconstruction performance metrics as input to predict design (specifically, electrode placement), proves challenging to train for intricate problems involving electrode placements on a 2D plane. This is due to the one-to-many mapping between the design and performance metric, wherein various combinations of electrode placements can yield an equivalent metric. [29]

The aim of this research is to introduce a systematic framework that employs a NN and an active learning-based optimization algorithm to optimize electrode placement for maximizing reconstruction performance concerning user-defined objectives.^[30] The proposed framework uses a surrogate model in the form of a forward modeling network that predicts performance metrics from electrode placement and subsequently performs optimization based on the surrogate model's predictions. This approach circumvents the challenges associated with inverse modeling networks that fail when multiple designs yield identical performance. Nevertheless, the proposed data-driven optimization has efficiency limitations when data gathering is time-consuming. In particular, the optimization of electrode placement for iterative reconstruction methods may be hindered by extended data collection periods. To overcome this issue, we propose the utilization of transfer learning to update the prediction model based on the NN. The model is initially trained using one-step reconstruction data, which requires a relatively shorter data collection time. Subsequently, the transferlearned model is utilized for the purpose of optimizing electrode placement for iterative reconstruction.

The article is structured as follows. The Experimental Section outlines the electrode placement optimization problems using two different reconstruction methods: the one-step reconstruction with Newton's one-step error reconstructor (NOSER) prior^[31] and the iterative total variation (TV) method. [32] The NOSER prior represents a linear methodology employed for expeditious image acquisition, whereas the iterative TV approach is employed in situations where additional time can be allocated to procure a sharp and precise image. For each reconstruction approach, three imagebased objective functions are defined and the optimal placements for each function are to be found. The study discusses how the aforementioned optimization problems can be effectively solved using active learning and transfer learning while comparing optimized results across different objectives and reconstruction methods. The outcomes of the problems are presented in Section 3, and the study's significance and limitations are discussed in Section 4.

2. Experimental Section

Optimization involves the task of selecting the optimal set of design variables to maximize or minimize objective functions while conforming to specified constraints.[33] In this study, considering the electrode placements as design variables, we must establish user-defined metrics as objective functions to quantify image reconstruction performances and take into account necessary constraints. This study seeks to determine optimized electrode placements for user-defined metrics related to position, size, and aspect ratio in image reconstruction, concerning two distinct reconstruction methods: one-step NOSER and iterative TV. Consequently, the Experimental Section delineates the following steps: 1) definition of the optimization problems; 2) optimization for one-step reconstruction; and 3) optimization for iterative reconstruction.

2.1. Definition of Optimization Problems

EIT is a technique used to estimate the conductivity distribution within a specific region through controlled current injection and voltage measurements from a limited number of electrodes. To achieve the conductivity reconstruction using EIT, both forward and inverse problems should be solved. The forward problem entails the measurement of voltages at electrodes for a given conductivity distribution, while the inverse problem involves reconstructing the conductivity field within the sensing domain based on the acquired voltage data.

To be specific, the objective of the forward problem is to compute the voltage field u on the boundary $\partial \Omega$, satisfying Equation (1), given a conductivity field σ within the domain $\Omega \subset \mathbb{R}^3$

$$\nabla \cdot (\sigma(\mathbf{x}) \nabla u(\mathbf{x})) = 0 \quad \mathbf{x} \in \Omega$$

$$\sigma(\mathbf{x}) \nabla u(\mathbf{x}) \cdot \mathbf{n} = j \qquad \mathbf{x} \in \partial \Omega$$
(1)

In Equation (1), j represents the current density, and n is the unit normal vector on $\partial\Omega$. The partial differential equation, derived from the Maxwell equation, is solvable through the finite element method (FEM).[34] The FEM resolves the equation based on specified parameters such as the number of electrodes, domain geometry, meshing method, injection and measurement patterns, and so on. Consequently, the voltage measured on the electrodes, denoted as $\Delta \nu_{m} \in \mathbb{R}^{L \times M},$ can be calculated for a perturbed conductivity field $\Delta \sigma_{\rm p} \in \mathbb{R}^{N_{\rm E} \times 1}$, where *L* is the number of electrodes, M is the number of measurement, and N_E is the number of elements in the finite element model, as expressed in Equation (2)

$$\Delta v_{\rm m} = F(\Delta \sigma_{\rm p}; \cdot) \tag{2}$$

Here, F represents the forward model, which is composed of the FEM simulation. For this study, we examined a scenario where electrodes are positioned on a single surface of the 3D thin plate domain. Each square element represents the values within a thin voxel. It is important to distinguish our case from conductivity imaging employing internal electrodes on a 2D surface. In the conductivity imaging, the formulation of the forward model F requires modification, diverging from that of EIT. [35,36] However, our study focuses on the 3D thin plate domain, where the model for solving the EIT forward problem remains applicable.

The inverse problem finds the reconstructed conductivity distribution $\Delta \sigma_{\rm r} \in \mathbb{R}^{N_{\rm E} \times 1}$ that minimizes the difference

ADVANCED ENGINEERING

www.advancedsciencenews.com www.aem-journal.com

between the measured voltage data $\Delta \nu_m$ and estimated voltage $\Delta \nu = F(\Delta \sigma,;)$ calculated from the defined forward model F. This is the difference of imaging methods, reconstructing the only $\Delta \sigma_r$ from the $\sigma_r = \sigma_0 + \Delta \sigma_r$, where the σ_0 is the reference conductivity field (uniform in this research), and σ_r is the total reconstructed conductivity field. The inverse problem can be formulated as follows

$$\Delta \sigma_{\mathbf{r}}(\cdot) = \underset{\Delta \sigma}{\operatorname{argmin}} [\|\Delta \nu_{\mathbf{m}} (\Delta \sigma_{\mathbf{p}}; \cdot) - F(\Delta \sigma; \cdot)\| + \alpha \|G(\Delta \sigma)\|]$$
 (3)

Here, $\|\cdot\|$ represents a predefined norm. G is the regularization term designed to compensate for the ill-posed nature of the inverse problem, and α is the weighting factor for the regularization term. The design of G aligns with the specific objectives; however, various conventional forms, including Tikhonov, [37] NOSER, [31] Laplac, [34] and TV, [32] have been proposed.

In this study, we specifically investigate the impact of electrode placement $X_e \in \mathbb{R}^{L \times 2}$ as a design variable

$$\Delta v = F(\Delta \sigma, X_e; \cdot) \tag{4}$$

The formulation of the inverse problem involves finding the $\Delta\sigma$ that corresponds to a measured voltage difference $\Delta\nu_{\rm m}$, as expressed in Equation (5)

$$\Delta\sigma_{\rm r}(X_{\rm e};\cdot) = \underset{\Delta\sigma}{\operatorname{argmin}}[\|\Delta\nu_{\rm m}(\Delta\sigma_{\rm p}, X_{\rm e};\cdot) - F(\Delta\sigma, X_{\rm e};\cdot)\| + \alpha \|G(\Delta\sigma)\|] \tag{5}$$

Error metrics and corresponding objective functions are necessary to quantify the discrepancy between the true conductivity field $\Delta\sigma_p$ caused by a perturbation and the reconstructed conductivity field $\Delta\sigma_r$.

When using EIT to reconstruct the conductivity drop of a single element, the resultant reconstructed image may exhibit deviations from the original one, as illustrated in Figure 1. To evaluate the fidelity of the reconstructed conductivity image, we created three image-based error measures: position error (PE), size error (SE), and aspect ratio error (ARE), drawing inspiration from previous research that developed image-based metrics for assessing the effi-cacy of the provided EIT system.^[18,38,39] While conventional metrics like peak-signal-to-noise ratio and structural similarity index measure exist for assessing reconstruction quality, [40] our aim was to devise metrics designed for specific engineering applications of EIT, such as crack detection and robotic skin, where an accurate description of position, size, and shape is crucial. Moreover, by formulating objective functions using metrics designed for engineering purposes, we identified that the proposed deep learning-based optimization framework can find the optimized configuration even for newly defined metrics by the user.

Defined metrics quantify the discrepancies between the reconstructed conductivity image and the originally perturbed element in terms of position, size, and aspect ratio. To ensure that calculations are based on positive values and to reduce the impact of excessive fluctuations far from the perturbation point, the errors are computed using the square of the reconstructed conductivity distribution. The normalized squared conductivity $(\Delta \widetilde{\sigma}_{r,i}^{P})^2$ for *i*th element, when perturbation occurred at the *p*th element, used in the error estimation, was computed using Equation (6)

$$\left(\widetilde{\Delta\sigma_{\mathbf{r},i}^{\mathbf{p}}}\right)^{2} = \frac{\left(\Delta\sigma_{\mathbf{r},i}^{\mathbf{p}}\right)^{2} - \min\left(\Delta\sigma_{\mathbf{r},i}^{\mathbf{p}}\right)^{2}}{\max\left(\Delta\sigma_{\mathbf{r},i}^{\mathbf{p}}\right)^{2} - \min\left(\Delta\sigma_{\mathbf{r},i}^{\mathbf{p}}\right)^{2}}$$
(6)

Here, $\Delta \sigma_{r,i}^p$ represents the reconstructed conductivity value for the ith element, while $\max\left(\Delta \sigma_{r,i}^p\right)^2$ and $\min\left(\Delta \sigma_{r,i}^p\right)^2$, respectively, indicate the maximum and minimum values of $\left(\Delta \sigma_{r,i}^p\right)^2$ across all elements.

To be specific, first, the PE quantifies the distance between the exact perturbation point (represented by a white "o" in Figure 1) and the center position of the reconstructed image derived from the squared conductivity values (indicated by a red "x" in Figure 1). The PE is defined as the magnitude of the vector connecting the center position of the reconstructed image $(\overrightarrow{r_c})$, and the center position of the perturbed element $(\overrightarrow{r_p})$. The equation for PE is given by

$$PE(p, X_e; \cdot) = \|\overrightarrow{\mathbf{r}_p} - \overrightarrow{\mathbf{r}_c}\|_2 = \left\|\overrightarrow{\mathbf{r}_p} - \frac{\sum_{i} \overrightarrow{r_i} \left(\Delta \widetilde{\sigma_{\mathbf{r}, i}^p}\right)^2}{\sum_{i} \left(\Delta \widetilde{\sigma_{\mathbf{r}, i}^p}\right)^2}\right\|_2$$
(7)

where $\overrightarrow{r_i}$ indicates the center position of the *i*th element. This concept is illustrated by the yellow vector connecting the red "x" and white "o", as described in Figure 1.

Second, SE characterizes the extent to which the reconstructed conductivity image diverges from the center. Drawing upon the intuitive notion derived from calculating the principal inertia moments of the mass distribution, we devised a method to quantify the deviation of the conductivity distribution from the center position. Using the centroid of the image as the origin, the inertia matrix for the conductivity distribution can be computed as outlined in Equation (8)

$$I_{\sigma^{2}}^{p} = \begin{bmatrix} I_{x'x'}^{p} & I_{x'y'}^{p} \\ I_{x'y'}^{p} & I_{y'y'}^{p} \end{bmatrix} = \begin{bmatrix} \sum_{i} \left(\widetilde{\Delta \sigma_{\mathbf{r}, i}^{p}} \right)^{2} y_{i}^{\prime 2} & \sum_{i} \left(\widetilde{\Delta \sigma_{\mathbf{r}, i}^{p}} \right)^{2} x_{i}^{\prime} y_{i}^{\prime} \\ \sum_{i} \left(\widetilde{\Delta \sigma_{\mathbf{r}, i}^{p}} \right)^{2} x_{i}^{\prime} y_{i}^{\prime} & \sum_{i} \left(\widetilde{\Delta \sigma_{\mathbf{r}, i}^{p}} \right)^{2} x_{i}^{\prime 2} \end{bmatrix}$$
(8)

 x_i' and y_i' represent the coordinates of the *i*th element along the x'-axis and y'-axis in Figure 1, respectively. The principal axes and inertia moments for the conductivity distribution can be obtained by solving an eigenvalue problem as illustrated in Equation (9)

$$\begin{bmatrix} I_{x'x'}^{p} & I_{x'y'}^{p} \\ I_{x'y'}^{p} & I_{y'y'}^{p} \end{bmatrix} [\mathbf{q}_{1} \quad \mathbf{q}_{2}] = [\mathbf{q}_{1} \quad \mathbf{q}_{2}] \begin{bmatrix} I_{\max}^{p} & 0 \\ 0 & I_{\min}^{p} \end{bmatrix}$$
(9)

Each of \mathbf{q}_1 and \mathbf{q}_2 represents the unit vector in the direction of the largest and smallest inertia moments, corresponding to the directions with the smallest and largest variance. Subsequently, I_{\min}^P and I_{\max}^P quantify how much the conductivity data spread along the vectors \mathbf{q}_1 and \mathbf{q}_2 , respectively. The coordinate system spanned by \mathbf{q}_1 and \mathbf{q}_2 is denoted as X' and Y', and its corresponding eigenvalues I_{\max}^P and I_{\min}^P are depicted in Figure 1. The geometric mean of the I_{\max}^P and I_{\min}^P is determined as the factor describing the deviation from the image centroid with respect to size, as outlined in Equation (10)

//onlinelibrary.wiley.com/doi/10.1002/adem.202301865 by Daegu Gyeongbuk Institute Of, Wiley Online Library on [18/09/2024]. See the Terms

and Conditions (https://onlinelibrary.wiley.com/terms-and-conditions) on Wiley Online Library for rules of use; OA articles are governed by the applicable Creative Commons

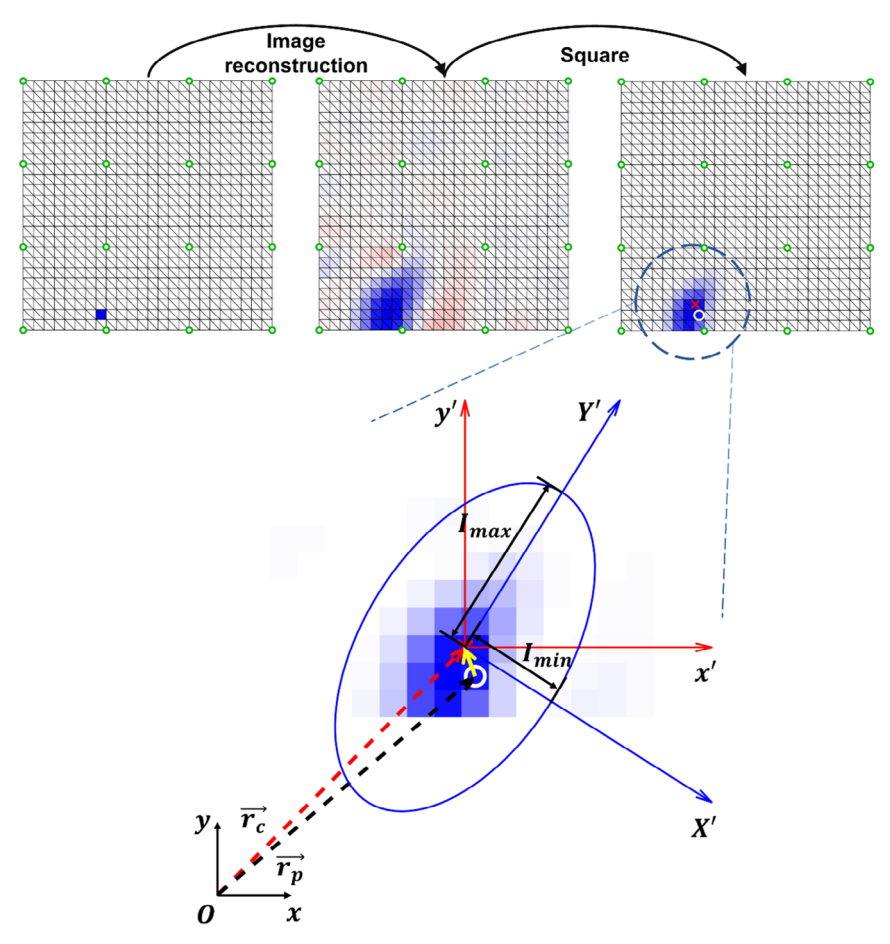


Figure 1. EIT-based image reconstruction with one-step NOSER regularization and the squared conductivity distribution for a single-element perturbation. The red "x" designates the center of the squared image, and the white "o" indicates the position of the perturbed element. The yellow vector illustrates the difference between the perturbation point and the reconstructed center. The blue ellipse visually represents the spread and aspect ratio distortion of the reconstructed image, with the major axis length denoted as I_{max} and the minor axis length as I_{min} .

$$SE(p, X_e; \cdot) = \sqrt{I_{\text{max}}^p \times I_{\text{min}}^p}$$
 (10)

The SE is related to the area of the blue ellipse in Figure 1. Finally, ARE calculates the degree of asymmetricity by using the ratio of I_{\max}^p and I_{\min}^p as defined in Equation (11)

$$ARE(p, X_e; \cdot) = \frac{I_{\text{max}}^p}{I_{\text{min}}^p}$$
(11)

The ARE is represented by the ratio between the major and minor axes of the blue ellipse in Figure 1. In other words, ARE quantifies the ratio of conductivity distribution variance between the two principal axes. It should be noted that the values of the three error measures are subject to change with the conductivity perturbation position and electrode placement.

The reconstruction performance of each electrode placement was quantified using three objective functions derived from the previously defined error metrics. These functions served as a metric for the optimization algorithm to determine the optimal electrode arrangements. To provide scalar values representing the reconstruction capability of each electrode placement, the

errors were assessed for all single-element perturbations and their average was computed. The average errors were modified to have values between $[0\,\infty)$ to yield higher values for better performance, which is characterized by precise center position, a sharp image like the original perturbation, and shape preservation. Table 1 summarizes the defined objective functions for the electrode configuration optimization.

To isolate the effect of the electrode placement on objective functions, other variables that could affect reconstruction quality, including the finite element model, reconstruction method, number of electrodes, and measurement pattern, were fixed. A 25×25 square grid model was used, and 16-point electrodes were placed on its nodes. First, the framework was applied to the one-step reconstruction method, the NOSER prior. While the one-step reconstruction method has lower accuracy than the iterative method, it was suitable for data-driven optimization because of its fast image restoration. In reconstruction calculations, the adjacent measurement pattern was used, and the regularization coefficient was set to 0.3. Additionally, based on the intuition that the optimal electrode placement exhibits symmetry, four electrodes are placed on a quarter of the plane, and the positions of the others are determined using axis symmetries. By

ns) on Wiley Online Library for rules of use; OA articles are governed by the applicable Creative Commons

www.advancedsciencenews.com www.aem-journal.com

Table 1. Three objective functions to assess the reconstruction performance of a given electrode placement (N_F = the number of elements).

	Mean of error	Objective function
Position objective function (POF)	$\overline{PE} = \frac{1}{N_E} \sum_{p=1}^{N_E} PE(p, X_e; \cdot)$	$POF(X_e; \cdot) = \frac{1}{\overline{PE}}$
Size objective function (SOF)	$\overline{SE} = \frac{1}{N_E} \sum_{p=1}^{N_E} SE(p, X_e; \cdot)$	$SOF(X_e; \cdot) = \frac{1}{\overline{SE}}$
Aspect ratio objective function (AOF)	$\overline{ARE} = \frac{1}{N_E} \sum_{p=1}^{N_E} ARE(p, X_e; \cdot)$	$AOF(X_e; \cdot) = \frac{1}{\overline{ARE} - 1}$

imposing symmetries on the example problem, we reduced the data generation time by perturbing only a quarter of the elements

2.2. Optimization for One-Step Reconstruction

In this study, an initial training dataset of 5000 instances was generated using the NOSER-based reconstruction method implemented in EIDORS.^[34] For each dataset, four electrode nodes were randomly selected within the lower-left quadrant of the finite element model, specifically within the region identified as the design space in **Figure 2a**. The symmetry principle was then applied to fill the remaining quadrants. After selecting

the electrode placements, individual elements within the design space underwent perturbation to assess errors. The resulting values were subsequently averaged over the number of elements within the design space to compute the objective functions as defined in the previous section. Consequently, each data pair consists of the positions of the four basis electrodes as input and the corresponding output values representing the objective functions. To incorporate the positional relationship between electrodes, the electrode placement information was transformed into a binary image format and fed into a convolutional NN. Specifically, the electrode placement information was embedded into a 12 by 12 binary image, where the nodes containing electrodes were represented by "1" and all other nodes by "0". Three separate networks were trained to predict each objective function value. The architecture of the NN and the input feature format are illustrated in Figure 2. The Adams optimizer was used to train the NN for 200 epochs with a minibatch size of 100. The learning rate was initially set to 10^{-3} and decreased by a factor of 10 every 20 epochs.

Deep NNs have limited accuracy when extrapolating beyond the initial training set, but they can still provide some performance ranking predictions for data near the training set. [30,41,42] To leverage this feature, we introduced a genetic algorithm that combines NN predictions and active learning to optimize electrode placement for each objective function. The initial dataset was sorted according to a performance metric, and the top 30 samples were selected as the parent generation. Crossover and mutation were applied to the parent generation to generate

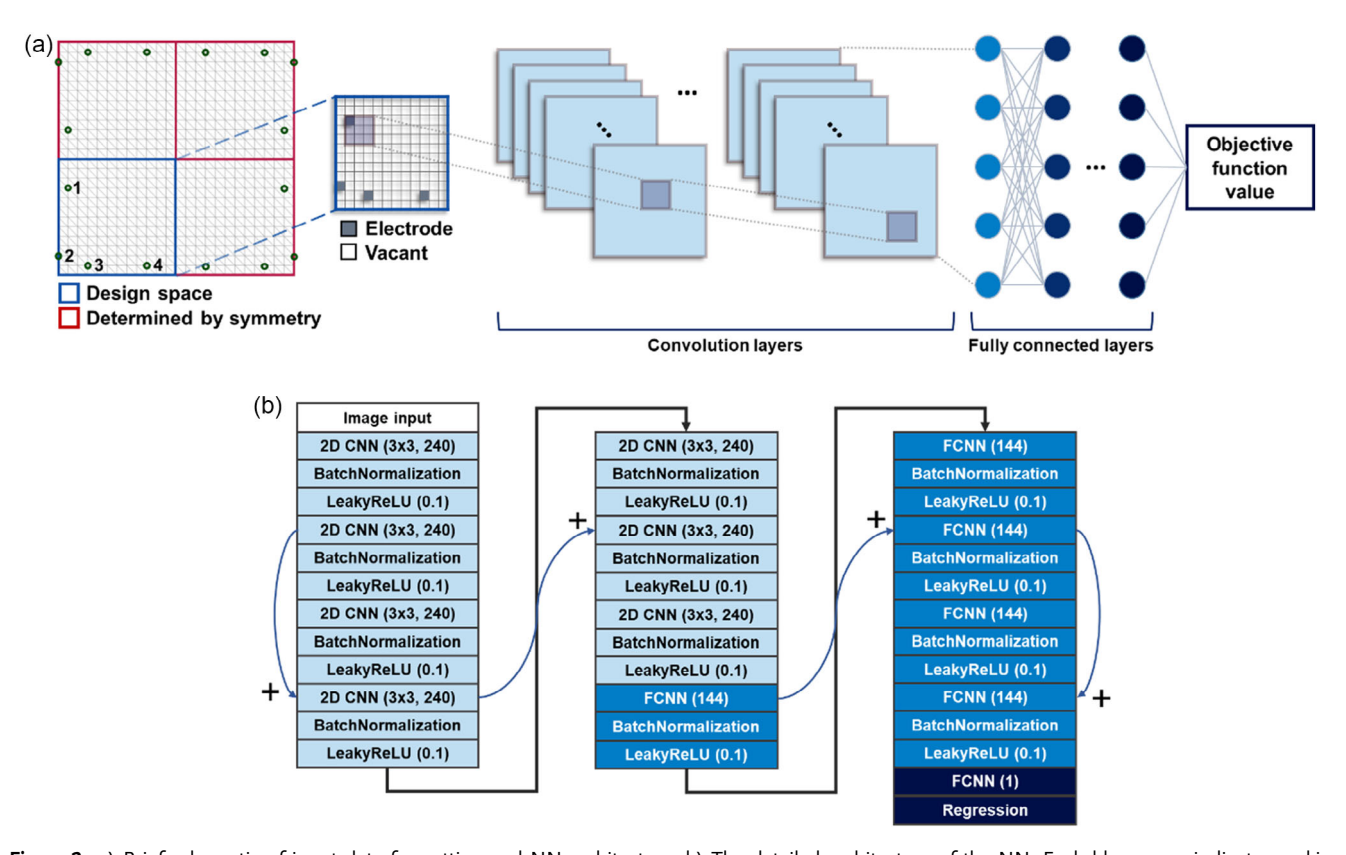


Figure 2. a) Brief schematic of input data formatting and NN architecture. b) The detailed architecture of the NN. Each blue arrow indicates a skip connection.

elibrary.wiley.com/doi/10.1002/adem.202301865 by Daegu Gyeongbuk Institute Of, Wiley Online Library on [18/09/2024]. See the Terms

and Conditions (https://onlinelibrary.wiley.com/terms-and-conditions) on Wiley Online Library for rules of use; OA articles are governed by the applicable Creative Commons

www.aem-journal.com

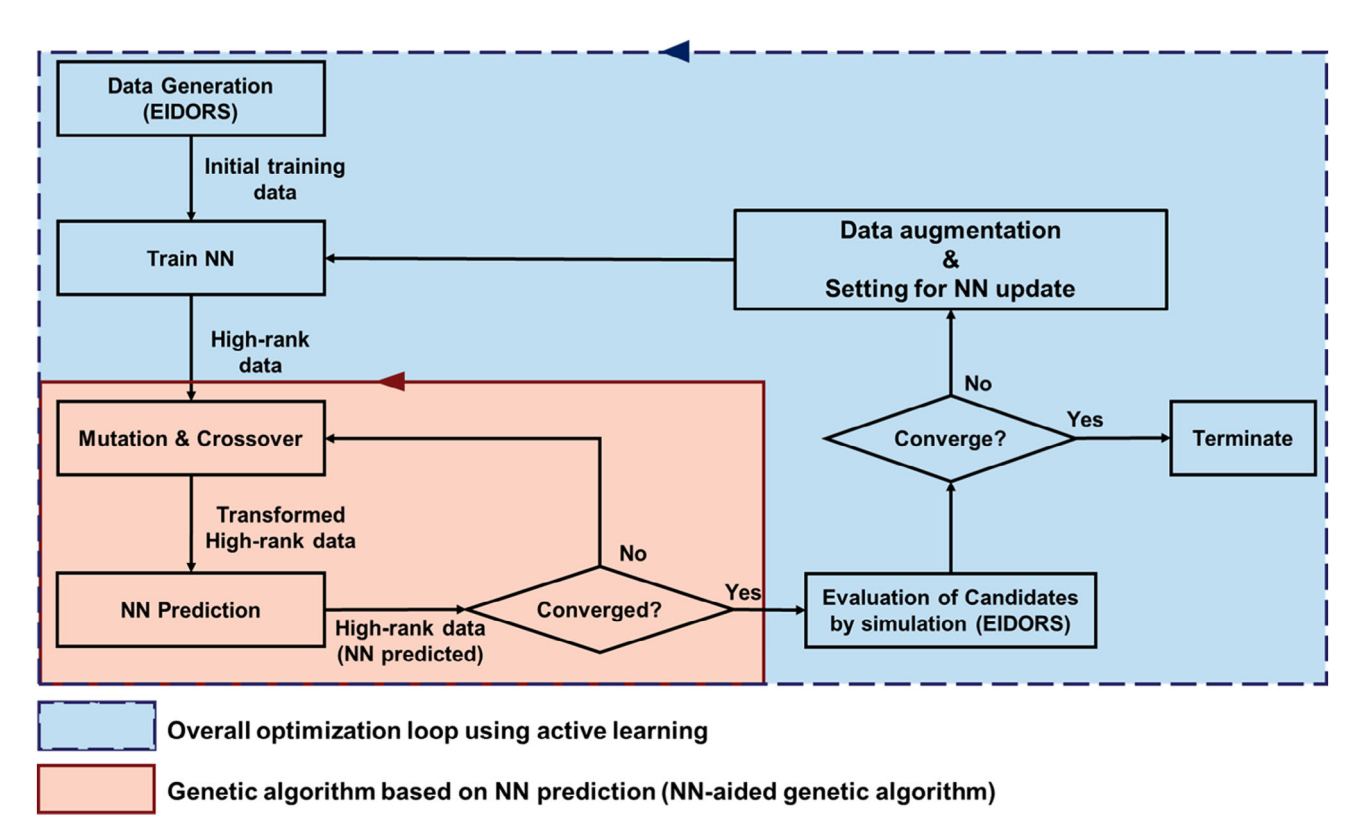


Figure 3. Schematic of the optimization procedure based on active learning.

approximately 10 000 new deformed samples in the offspring generation. The offspring group's objective function values were predicted using NN and sorted in descending order to select the top 30 placements as the next parental generation. The red loop in **Figure 3** illustrates the NN-aided genetic algorithm process described above. The genetic algorithm had a population size of 200, with each individual consisting of 4 integers to represent electrode placement. The schematic of mutation and crossover utilized in this study is presented in the Supporting Information (see Supporting Notes 2). The mutation probability and crossover probability were set high, nearly 0.9 and 1.0, respectively, to explore various design candidates with the rapid prediction of the NN. The process continued until convergence, defined as no longer changing in the highest value for three generations.

The selected electrode placements were utilized to update the NNs, resulting in enhanced prediction accuracy for high-performance placements, which were then used to predict the next iteration in the active learning-based algorithm. To be specific, the true objective function values of the converged parental generations were evaluated using EIDORS, and the resulting data pairs were added to the initial training set to augment the dataset and update the NN. The entire process, from the NN-aided genetic algorithm to the NN update, was repeated until no improvement was observed for four iterations, in a process known as active learning-based optimization (the blue loop in Figure 3). It is known that the algorithm's ability to rapidly evaluate input features through NNs allows it to outperform traditional genetic algorithms. [43]

2.3. Optimization for Iterative Reconstruction

The optimization methodology used for one-step reconstruction can be applied to an iterative reconstruction, TV-based datasets. However, we encountered a challenge in training NNs with a large dataset due to the time-consuming computation required for iterative reconstruction. While the superiority of TV in terms of both POF and SOF was noted, the proposed algorithm was not feasible due to these computational limitations. To address this issue, we employed a transfer learning approach by updating pretrained NOSER data-based NNs with a small number of iterative TV-based data to construct a predictive model for iterative reconstruction. This approach allowed us to reduce the time required to train the model while maintaining its accuracy. For instance, generating 5000 data using iterative TV can take up to 2 weeks, while the same amount of data using one-step NOSER can be generated in 7 h (Table 2). The calculations were performed

Table 2. Comparison of computing time and objective function values between two reconstruction methods: one-step NOSER and iterative TV.

One-step NOSER	Iterative TV
5	250
11.0570	30.8530
0.9202	6.1107
1.6734	0.4516
	0.9202

ADVANCED SCIENCE NEWS ADVANCED ENGINEERING MATERIALS

www.aem-journal.com

www.advancedsciencenews.com

using MATLAB R2022a running on a desktop computer with an Intel Core i7-10700 K processor and 128 GB of DDR4 RAM.

To implement the transfer learning-based approach, we generated a set of 300 TV-based data samples, which were used to update the pretrained NN with the NOSER-based dataset. We used the EIDORS to implement the iterative TV-based EIT calculation, using the same finite element model as the NOSER section, with a regularization coefficient of 10^{-5} . In the transfer learning phase, we made minor modifications to the hidden layer weights, with an initial learning rate and epoch of 10^{-3} and 50, respectively. The learning rate was reduced by a factor of 10 every 10 epochs, and the minibatch size was 5. The NN architecture was identical to the one described in the NOSER section, as illustrated in Figure 2b. Other training options were maintained from the previous problem for one-step reconstruction. To monitor the training progress of transfer learning, refer to the loss curve in the Supporting Information (see Supporting Notes 1). The transfer-learned NN was then employed to optimize electrode placements using a genetic algorithm, following a similar approach to the previous section. The optimization process was stopped when there was no improvement for four iterations, consistent with the previous section's criteria.

3. Results and Discussion

The proposed active learning-based optimization approach relies on the NNs' ability to extrapolate beyond the training domain. The trained NNs using a lower 90% rank dataset were tested on the top 10% highest rank dataset to evaluate their predictive capacity beyond the training data, as shown in **Figure 4**a. The predicted values for the POF and SOF outcomes closely approximate the actual data trend. However, for the AOF, its accuracy is comparatively lower than the other two functions. Nevertheless, the overall performance of the three trained NNs is adequate to distinguish whether an electrode placement is superior to the training data samples.

The electrode configurations with high objective function values were updated following the proposed design progress, which included the NN-aided genetic algorithm and NN update using superior data samples. Figure 4b shows the distribution of the top 30 datasets selected by the genetic algorithm and evaluated by EIDORS at each iteration. As the number of iterations increased, the NN was gradually updated with the superior samples, leading to an improvement in the prediction accuracy for the upper ranks. For the one-step reconstruction, the NNs were not updated several times because they already exhibited sufficient extrapolation accuracy to replace the simulation. The percentage of the improvement (PI) estimated by Equation (4) was 6.19%, 13.15%, and 14.48% for each objective function. The improvement for each iteration can be found in the Supporting Information (see Supporting Notes 3).

$$PI = \frac{\text{Initial best value} - \text{Optimized value}}{\text{Initial best value}} \times 100(\%) \tag{12}$$

Figure 4c depicts the optimal electrode placements for the three objective functions, indicating that uniformly distributed electrodes across all domains resulted in improved image reconstruction accuracy. However, it is noteworthy that the optimal

placements slightly vary for different objective functions, which depends on the primary focus of the EIT application. These results show the significance of considering a user-defined specific objective while determining the electrode placement.

To implement the optimization for the iterative reconstruction, transfer learning was carried out by using 300 iterative TV data to update NNs previously trained with 5000 one-step NOSER data to make predictions for iterative TV. To check the extrapolation capacity of the transfer-learned NN, the 300 data were split into a 95% training set and a 5% test set, and the test results are presented in **Figure 5**a. The NN for the AOF tended to underestimate the test set, while the NNs for the POF and SOF provided better predictions, although not perfect. These results confirm that the POF and SOF are less sensitive to the change in the reconstruction method.

Following the active learning-based optimization strategy, the electrode arrangement design was gradually improved (Figure 5b). As the number of iterations increases, the NN was updated, resulting in an improvement in the predictive ability for higher-ranked data. Notably, for the AOF, whose extrapolation capability was initially inadequate, there was a significant enhancement in the NN's predictive power for the dataset outside the initial region. Conversely, the NNs for the PDF and SOF showed less improvement than AOF, as they initially had better extrapolation performance.

The optimization algorithm was executed for 18, 6, and 18 iterations for each objective function. Unlike optimization in the one-step NOSER, the highest value drops in the middle of the optimization process (see Supporting Notes 3). This is a case where the actual performance calculated by EIDORS was not that outstanding even though they are recommended as the superior placements based on the NN-aided genetic algorithm. This occurred because the extrapolation power of iterative reconstruction is lower than that of one-step reconstruction. Nevertheless, the proposed optimization eventually converged to a certain value and identified placements with superior performance compared to the initial best. The percentage improvement for each objective function was 20.13%, 1.39%, and 16.12%.

The optimal electrode arrangements are presented in Figure 5c. It was observed that a uniform distribution of electrodes throughout the domain was optimal for the SOF. Conversely, for the POF, the optimal electrode placement was found to be toward the boundary of the domain. In the case of AOF, the optimal one was difficult to infer intuitively. We discovered that finding the optimal electrode placement could be challenging in some instances and necessitate a data-driven optimization approach. In addition, for all three objective functions, the optimization results differed from the optimum obtained in the one-step reconstruction depicted in Figure 4c. Therefore, it was confirmed that optimal electrode arrangement can vary not only depending on the objective function but also on the chosen reconstruction methodology.

To validate the enhanced accuracy of optimized electrode placements (referred to as "opt") in comparison with conventional electrode arrangements, we established two reference electrode configurations for comparison. These included a commonly employed uniform arrangement (referred to as "uni") and an arrangement with electrodes uniformly distributed along the boundary (referred to as "bnd"), as depicted in **Figure 6**a. We

15272648, 2024, 11, Downloaded from https://onlinelibrary.wiley.com/doi/10.1002/adem.202301865 by Daegu Gyeongbuk Institute Of, Wiley Online Library on [1809/2024]. See the Terms

ons) on Wiley Online Library for rules of use; OA articles are governed by the applicable Creative Commons!

www.aem-journal.com

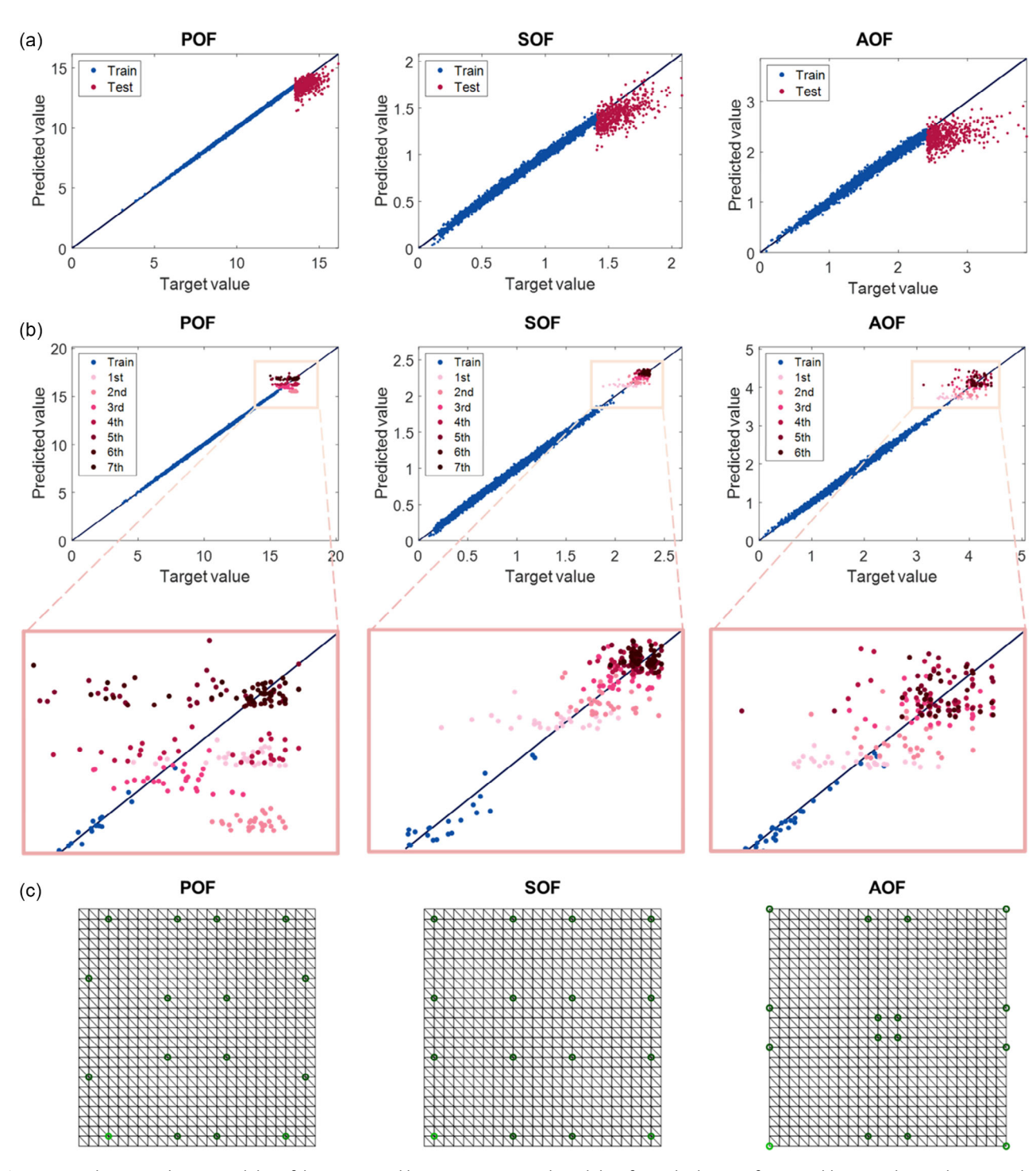


Figure 4. a) The extrapolation capability of the NN trained by one-step NOSER-based data for each objective function (blue: 90% low-rank training data, red: 10% high-rank test data). b) Predicted and target values of objective functions of the top 30 placements selected by NN-aided genetic algorithm for each iteration (one-step NOSER). c) Optimal electrode placements for defined objective functions (one-step NOSER).

computed the PE, SE, and ARE for a total of 576 elements for both "uni" and "bnd," using both the one-step and iterative reconstruction methods. These calculations were then compared with the element-wise errors for the corresponding optimized electrode placements. The distribution of calculated errors for each electrode placement is visualized as histograms in Figure 6b. The

results consistently demonstrated a trend in which the gray distribution representing errors for the optimized placements in each case shifted toward lower values. This shift is further highlighted by bold vertical lines representing the mean of each distribution, and in all cases, these means moved toward lower error values. These findings indicate that electrode placements optimized based

15272648, 2024, 11, Downloaded from https:/

onlinelibrary.wiley.com/doi/10.1002/adem.202301865 by Daegu Gyeongbuk Institute Of, Wiley Online Library on [18/09/2024]. See the Terms.

ons) on Wiley Online Library for rules of use; OA articles are governed by the applicable Creative Commons I

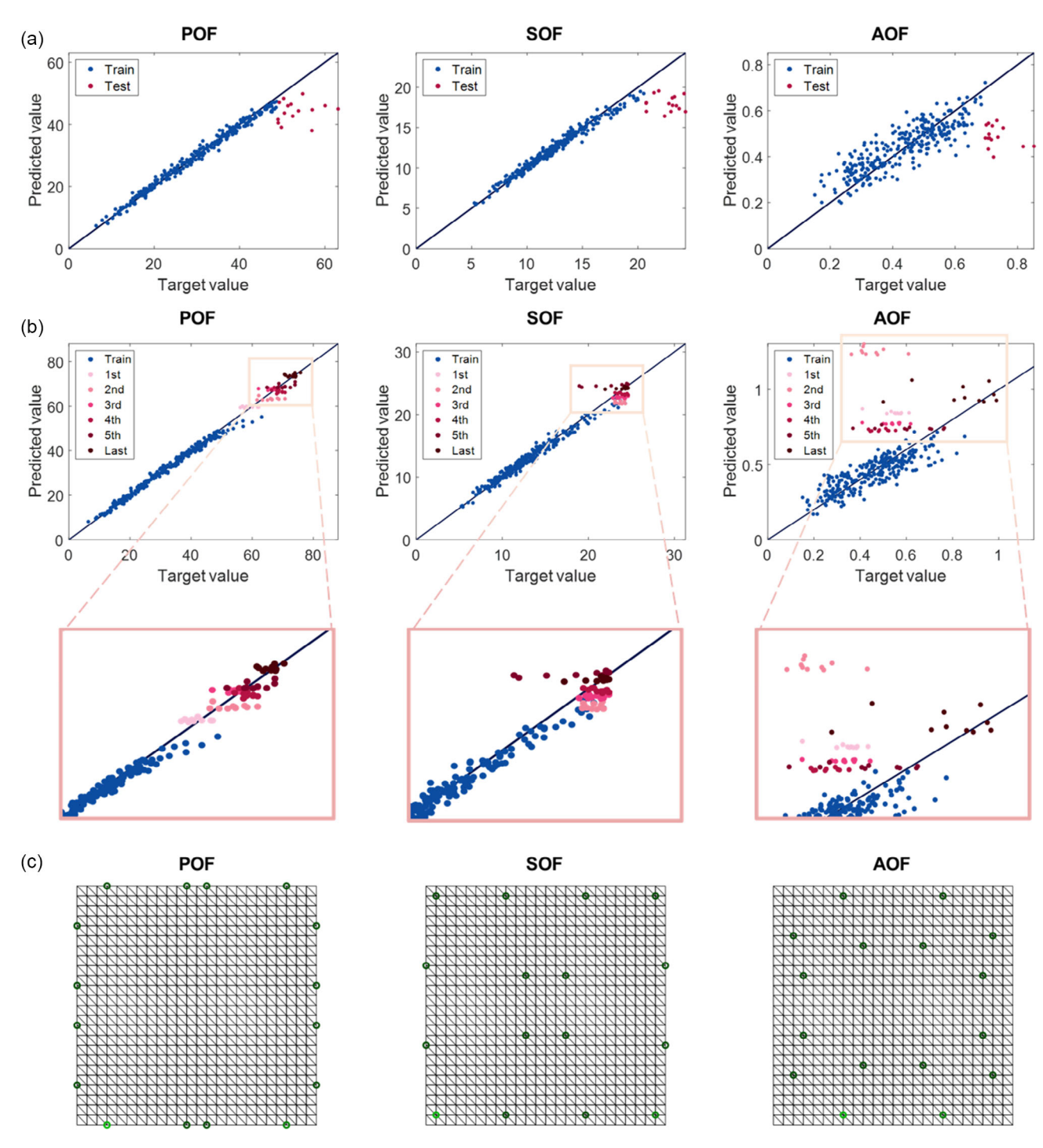


Figure 5. a) The extrapolation capability of the NN trained by iterative TV-based data for each objective function (blue: 95% low-rank training data, red: 5% high-rank test data). b) Predicted and target values of objective functions of the top 30 placements selected by NN-aided genetic algorithm for each iteration (iterative TV). c) Optimal electrode placements for defined objective functions (iterative TV).

on the active learning-based framework exhibited higher accuracy compared to common electrode placements.

Furthermore, we observed variations in reconstructed images and their associated error values in response to changes in electrode placement. To intuitively grasp the relationship between error and the reconstructed image, we began by selecting a single

element that effectively shows the changes in image reconstruction with respect to defined errors and applied a conductivity perturbation. Subsequently, we compared the differences in the restored conductivity images and their error values for various electrode placements, including uniform placement, boundary placement, and electrode placements optimized for each

and Conditions (https://onlinelibrary.wiley.com/terms

and-conditions) on Wiley Online Library for rules of use; OA articles are governed by the applicable Creative Commons

www.advancedsciencenews.com www.aem-journal.com

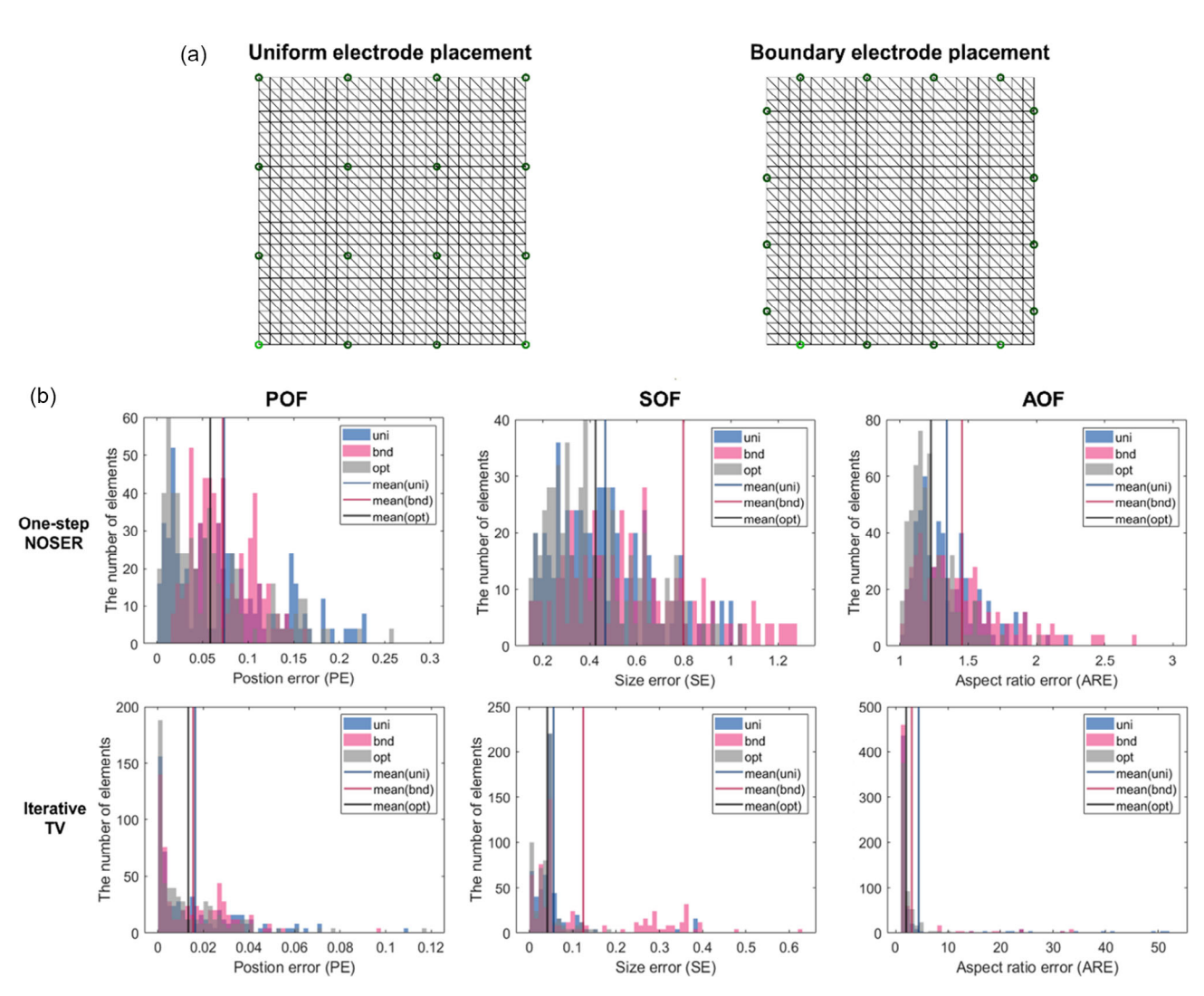


Figure 6. a) Comparison of uniform and boundary electrode placements for assessing accuracy against optimized electrode placements. b) Error distribution for the uniform electrode placement (uni), the boundary electrode placement (bnd), and the optimized electrode placement for each objective function (opt). Vertical lines represent the mean estimated errors for all elements in the domain associated with each electrode placement.

objective function. The two image reconstruction methods used in this study, one-step NOSER and iterative TV, were employed for each electrode placement, and the reconstruction outcomes for each scenario are illustrated in Figure 7.

In general, it was evident that, despite applying perturbations to elements at the same location, the error values vary depending on the electrode placement. Specifically, when examining the PE, the distance between the white "o", representing the position of the single-element perturbation, and the center of the restored image indicated by the red "x" increases with the corresponding increase in PE. Regarding the SE, as the reconstructed image deviates from the center of the image, the SE value increases. Comparing the response from perturbing the element located at the center of the domain, it is observed that the SE is higher when electrodes are present only at the boundary. In the optimized electrode placement, superior reconstruction performance is achieved for the element positioned at the center compared to uniform placement. The ARE decreases as the

reconstructed image for the element located at the edge becomes more circular. Assuming the original single-element perturbation is square-shaped, a higher ARE suggests a more significant shape distortion in the reconstructed image.

However, the optimization in this study did not target the enhancement of the reconstruction accuracy for a specific individual element perturbation. Instead, it focused on optimizing the overall single-element perturbation errors across all elements. Consequently, it was essential to visualize the error values corresponding to single-element perturbations for all elements and confirm whether the optimization had indeed improved the overall distribution of these errors. The distribution of each error value, encompassing PE, SE, and ARE, for uniform, boundary, and optimized electrode placements for each objective function is depicted in Figure 8. This enables a more in-depth analysis compared to the histogram presented in Figure 6.

Overall, following optimization for each objective function, the optimized electrode configurations exhibit a smaller average

nelibrary.wiley.com/doi/10.1002/adem.202301865 by Daegu Gyeongbuk Institute Of, Wiley Online Library on [18/09/2024]. See the Terms

are governed by the applicable Creative Commons

www.aem-journal.com

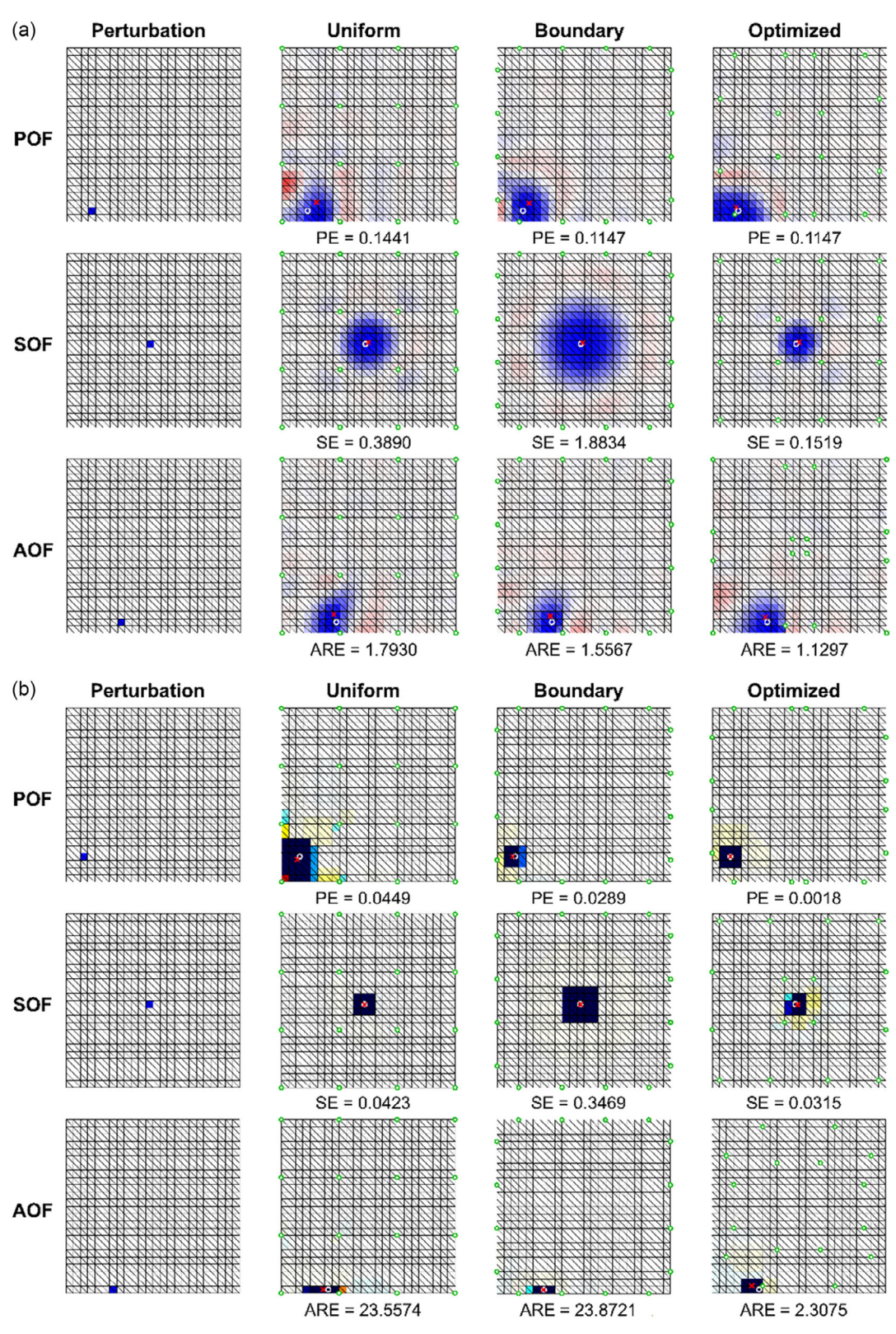


Figure 7. Single-element conductivity perturbations and their respective reconstructed conductivity images are displayed for each electrode placement (uniform, boundary, and optimized). The positions of electrodes are indicated by a green "o", the original perturbation point is marked as a white "o", and the center of the reconstructed image is represented by a red "x". Corresponding error values for each reconstructed image are presented below the images: a) one-step NOSER, and b) iterative TV.

//onlinelibrary.wiley.com/doi/10.1002/adem.202301865 by Daegu Gyeongbuk Institute Of, Wiley Online Library on [18/09/2024]. See the Terms

on Wiley Online Library for rules of use; OA articles are governed by the applicable Creative Commons

www.aem-journal.com

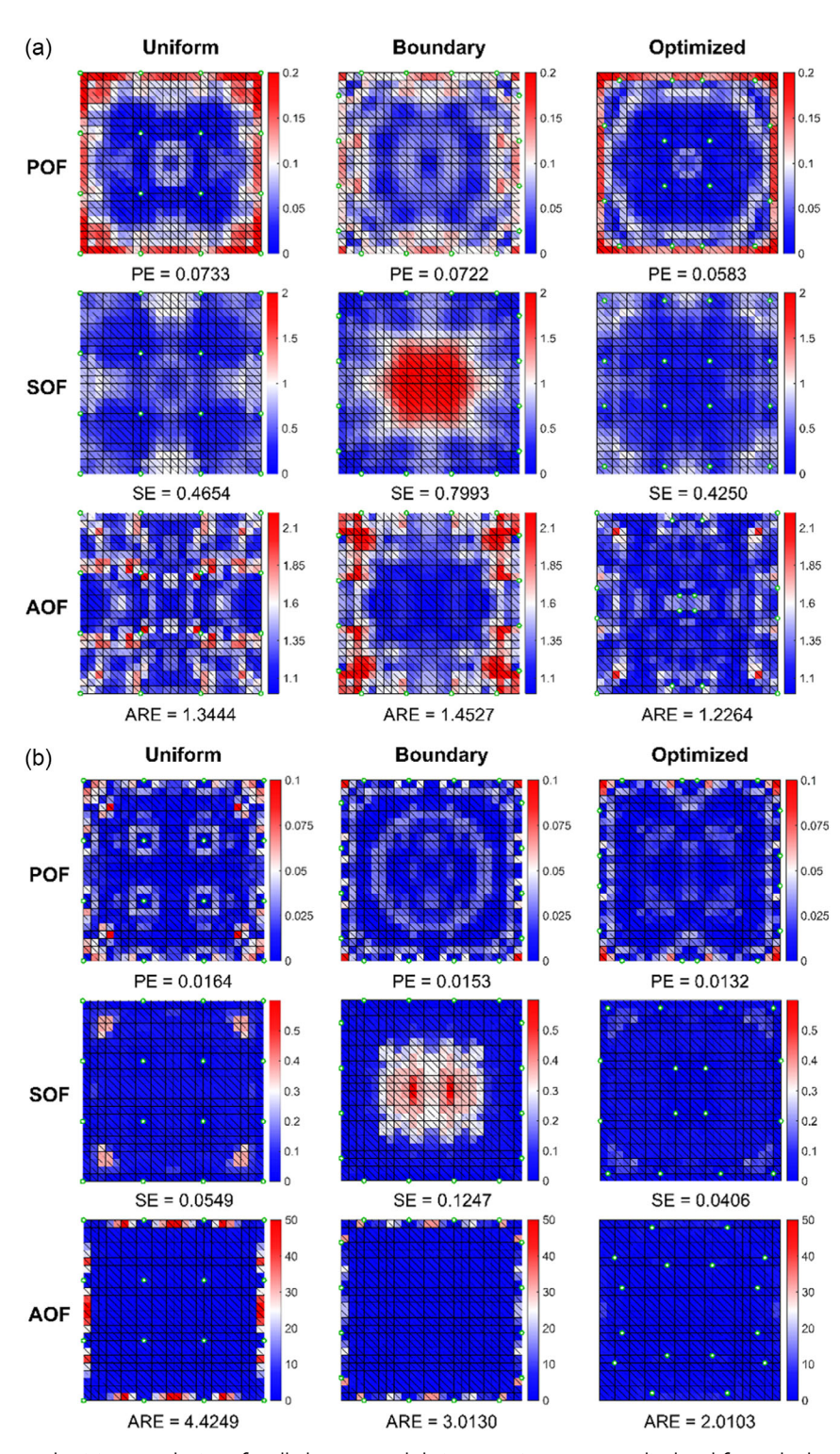


Figure 8. Single-element conductivity perturbations for all elements and their respective errors are displayed for each electrode placement (uniform, boundary, and optimized). Corresponding average error values for each electrode placement are provided beneath the images: a) one-step NOSER, and b) iterative TV.

error compared to the uniform and boundary placements. For POF, it was observed that the optimization reduced errors appearing in the corners for the uniform placement and generally evened out errors across the entire map for the boundary placement. Regarding SOF, there was notable improvement in errors located at the domain center compared to the boundary

ADVANCED SCIENCE NEWS ADVANCED ENGINEERING MATERIALS

www.advancedsciencenews.com www.aem-journal.com

placement, and enhancement was evident for elements with errors in the uniform placement. Similarly, for AOF, errors near corners and edges were noticeably reduced with optimization. Particularly, for iterative TV, it was effective in significantly lowering errors occurring at the edges. In conclusion, the proposed deep learning-based optimization framework demonstrates effective optimization for image reconstruction corresponding to single-element perturbation across all elements.

4. Conclusion

This study proposes an optimization framework for electrode placement in the EIT using active learning, data augmentation, and transfer learning. The proposed framework optimizes electrode placements on 2D planes by leveraging an NN-based algorithm to approach optimal designs for user-defined objective functions and specified reconstruction setups.

For the one-step NOSER reconstruction, this study identified optimal electrode placements to accurately restore perturbation position, size, and aspect ratio. NNs were trained to predict three objective function values that quantify the imaging accuracy of electrode placements, demonstrating sufficient extrapolation ability beyond the training domain. Active learning-based optimization improved image quality by 6.19%, 13.15%, and 14.48% from the initial best placement performance, with optimal electrode placements evenly distributed throughout the target domain.

Furthermore, a transfer learning approach was employed to address the time-consuming data collection process for constructing a prediction model for the iterative TV dataset. Although the accuracy of NN predictions beyond the initial training range was lower than that of one-step reconstruction, it was still sufficient for the proposed optimization strategy to be applied. The study successfully identified optimal electrode placements for each defined objective function, resulting in an improvement in imaging performance by 20.13%, 1.39%, and 16.12% from the initial best design. The study successfully determined optimal electrode placements for each defined objective function, resulting in imaging performance improvements of 20.13%, 1.39%, and 16.12% from the initial best design. Optimal electrode placements were toward the boundary for the POF and evenly distributed for the SOF. However, for the AOF, optimal placement was difficult to predict and could only be obtained through data-driven optimization.

However, the improvement in EIT performance through electrode placement optimization was not as substantial compared to the impact of altering other factors, such as reconstruction methods and the number of electrodes. Therefore, electrode placement optimization can be viewed as a fine-tuning process after appropriately selecting and optimizing other factors. Moreover, as the optimization results relied solely on simulation data under ideal conditions, actual situations with error factors may produce disparities. Future research should consider developing electrode placement design methodologies that account for differences between simulation and experimental data.

Nonetheless, the proposed optimization framework offers benefits for engineers seeking to optimize EIT performance in specific environments. As this study identifies optimal electrode placements using NNs, it can be extended to other optimization problems with various problem settings, such as geometry, meshing, measurement pattern, reconstruction method, and type of electrodes, provided that data are available and NNs are trainable. Additionally, the study demonstrates the potential of transfer learning to accelerate the optimization process for different options once one of them has been solved.

Supporting Information

Supporting Information is available from the Wiley Online Library or from the author.

Acknowledgements

This work was financially supported by the National Research Foundation of Korea (NRF) (grant no. 2022R1A2B5B02002365) and the Nanomedical Devices Development Project of NNFC in 2023.

Conflict of Interest

The authors declare no conflict of interest.

Data Availability Statement

The data that support the findings of this study are available from the corresponding author upon reasonable request.

Keywords

data-driven optimization, electrical impedance tomography, machine learning

Received: November 8, 2023 Revised: March 20, 2024 Published online: April 25, 2024

- [1] B. H. Brown, J. Med. Eng. Technol. 2003, 27, 97.
- [2] M. Cheney, D. Isaacson, J. C. Newell, SIAM Rev. 1999, 41, 85.
- [3] T. N. Tallman, S. Gungor, K. Wang, C. E. Bakis, Struct. Health Monit. 2015, 14, 100.
- [4] W. Lestari, B. Pinto, V. La Saponara, J. Yasui, K. J. Loh, Smart. Mater. Struct. 2016, 25, 085016.
- [5] H. Park, H. Lee, K. Park, S. Mo, J. Kim, in 2019 IEEE/RSJ Int. Conf. on Intelligent Robots and Systems (IROS), IEEE, Macau 2019.
- [6] K. Park, H. Yuk, M. Yang, J. Cho, H. Lee, J. Kim, Sci. Robot. 2022, 7, eabm7187.
- [7] B. R. Loyola, V. La Saponara, K. J. Loh, T. M. Briggs, G. O'Bryan, J. L. Skinner, *IEEE Sens. J.* 2013, 13, 2357.
- [8] T.-C. Hou, K. J. Loh, J. P. Lynch, Nanotechnology 2007, 18, 315501.
- [9] T. Tallman, S. Gungor, K. Wang, C. E. Bakis, Smart. Mater. Struct. 2014, 23, 045034.
- [10] T.-C. Hou, J. P. Lynch, J. Intell. Mater. Syst. Struct. 2009, 20, 1363.
- [11] M. Hallaji, M. Pour-Ghaz, NDT E Int. 2014, 68, 13.
- [12] D. Smyl, M. Pour-Ghaz, A. Seppänen, NDT E Int. 2018, 99, 123.
- [13] G. Rao, M. A. Sattar, R. Wajman, L. Jackowska-Strumiłło, Sensors 2021, 21, 564.

ADVANCED SCIENCE NEWS ADVANCED ENGINEERING

www.advancedsciencenews.com www.aem-journal.com

- [14] H. Ghaednia, C. E. Owens, R. Roberts, T. N. Tallman, A. J. Hart, K. M. Varadarajan, Smart. Mater. Struct. 2020, 29, 085039.
- [15] H. Hassan, T. Tallman, in Sensors and Smart Structures Technologies for Civil, Mechanical, and Aerospace Systems 2020, SPIE, CA, United States 2020.
- [16] K. Park, H. Lee, K. J. Kuchenbecker, J. Kim, IEEE ASME Trans. Mechatron. 2021, 27, 304.
- [17] E. Ravagli, S. Mastitskaya, N. Thompson, K. Aristovich, D. Holder, Physiol. Meas. 2019, 40, 115007.
- [18] S. Russo, S. Nefti-Meziani, N. Carbonaro, A. Tognetti, Sensors 2017, 17, 1999.
- [19] K. Park, J. Kim, IEEE Trans. Robot. 2022, 38, 3463.
- [20] D. Smyl, D. Liu, IEEE Trans. Instrum. Meas. 2020, 69, 6030.
- [21] A. Karimi, L. Taghizadeh, C. Heitzinger, Comput. Methods Appl. Mech. Eng. 2021, 373, 113489.
- [22] S. Vergara, D. Sbarbaro, T. A. Johansen, Meas. Sci. Technol. 2017, 28, 084003.
- [23] Z. Zhao, I. Frerichs, S. Pulletz, U. Müller-Lisse, K. Möller, J. X-Ray Sci. Technol. 2014, 22, 797.
- [24] S. Leonhardt, A. Cordes, H. Plewa, R. Pikkemaat, I. Soljanik, K. Moehring, H. J. Gerner, R. Rupp, Biomed. Eng.-Biomed. Tech., 2011, 56, 301.
- [25] A. K. Khambampati, S. K. Konki, Y. Han, S. Sharma, K. Y. Kim, in TENCON 2018-2018 IEEE Region 10 Conf., IEEE, Jeju Island, Korea 2018.
- [26] J. Avery, M. Runciman, C. Fiani, E. M. Sanchez, S. Akhond, Z. Liu, K. Aristovich, G. Mylonas, in 2022 IEEE/RSJ Int. Conf. on Intelligent Robots and Systems (IROS), IEEE, Kyoto, Japan 2022.
- [27] D. Liu, D. Gu, D. Smyl, J. Deng, J. Du, IEEE Trans. Med. Imaging 2020, 39, 2954.

- [28] W. R. Lionheart, Physiol. Meas. 2004, 25, 125.
- [29] J. Lee, D. Park, M. Lee, H. Lee, K. Park, I. Lee, H. Lee, K. Park, I. Lee, S. Ryu, Mater. Horiz. 2023, 10, 5436.
- [30] Y. Kim, Y. Kim, C. Yang, K. Park, G. X. Gu, S. Ryu, npj Comput. Mater. 2021, 7, 140.
- [31] M. Cheney, D. Isaacson, J. C. Newell, S. Simske, J. Goble, Int. J. Imaging Syst. Technol. 1990, 2, 66.
- [32] A. Borsic, B. M. Graham, A. Adler, W. R. Lionheart, IEEE Trans. Med. Imaging 2009, 29, 44.
- [33] J. Arora, in Introduction to Optimum Design, Elsevier, New York 2004.
- [34] A. Adler, W. R. Lionheart, Physiol. Meas. 2006, 27, S25.
- [35] C. Hähnlein, K. Schilcher, C. Sebu, H. Spiesberger, Inverse Probl. Sci. Eng. 2011, 19, 729.
- [36] B. Jin, X. Li, Q. Quan, Z. Zhou, SIAM J. Imaging Sci. 2024, 17, 147.
- [37] M. Vauhkonen, D. Vadász, P. A. Karjalainen, E. Somersalo, J. P. Kaipio, IEEE Trans. Med. Imaging 1998, 17, 285.
- [38] C. Xu, X. Dong, X. Shi, F. Fu, W. Shuai, R. Liu, F. You, in 2008 2nd Int. Conf. on Bioinformatics and Biomedical Engineering, IEEE, Sanghai, China 2008.
- [39] M. Yasin, S. Böhm, P. O. Gaggero, A. Adler, *Physiol. Meas.* 2011, 32, 851
- [40] A. Hore, D. Ziou, in 2010 20th Int. Conf. on Pattern Recognition, IEEE, Istanbul, Turkey 2010.
- [41] G. Martius, C. H. Lampert, in 5th Int. Conf. Learn. Represent (ICLR), Toulon, France 2016.
- [42] E. Barnard, L. Wessels, IEEE Control Syst. 1992, 12, 50.
- [43] S. Lee, W. Choi, J. W. Park, D.-S. Kim, S. Nahm, W. Jeon, G. X. Gu, M. Kim, S. Ryu, *Nano Energy* **2022**, *103*, 107846.